Nonlinear wave interactions on the surface of a conducting fluid under vertical electric fields

Tao Gao[a], Zhan Wang[b,c,*], Jean-Marc Vanden-Broeck[d,*]

[a]*Department of Mathematical Sciences, University of Essex, Wivenhoe Park, Colchester CO4 3SQ, UK*
[b]*Institute of Mechanics, Chinese Academy of Sciences, Beijing 100190, China*
[c]*School of Engineering Science, University of Chinese Academy of Sciences, Beijing 100049, China*
[d]*Department of Mathematics, University College London, WC1E 6BT, UK*

Abstract

In this paper, we are concerned with capillary-gravity waves propagating on a two-dimensional conducting fluid under the effect of an electric field imposed in the direction perpendicular to the undisturbed free surface. This work aims to investigate the impact of the electric fields on the nonlinear wave interactions in this context. The full system is mathematically difficult to solve since it is a nonlinear, two-layered, free boundary problem, and the interface dynamics results from the strong coupling between the Euler equations for the lower fluid layer and an electric contribution from the upper gas layer. To investigate electrohydrodynamic wave interactions, we propose a novel numerical scheme based on a time-dependent conformal map and an interpolation technique to conduct unsteady simulations of the fully nonlinear electrified Euler equations of the two-layered problem. To gain analytical insights, we first derive weakly nonlinear envelope equations based on the method of multiple scales for the resonant triad, long-short wave interaction, and modulation of a single-mode wavetrain (a special case of resonant quartet interaction). Summative remarks are made to illustrate the transition from 3-wave interactions to 4-wave interactions and vice versa, occurring when the coefficients of the associated nonlinear Schrödinger equation become singular. The fully nonlinear results obtained by the prescribed numerical method are compared with the predictions by the weakly nonlinear theories, and good agreement is achieved.

Keywords: wave interactions, gravity-capillary waves, electrohydrodynamics

*Corresponding author
Email addresses: zwang@imech.ac.cn (Zhan Wang), j.vanden-broeck@ucl.ac.uk (Jean-Marc Vanden-Broeck)

1. Introduction

Electrohydrodynamics (EHD) is a cross-discipline subject that considers the coupling interplay between fluids and electric fields. It is easy to artificially manipulate considerably strong electric fields with modern engineering techniques to cause significant changes in fluid motion, usually manifested via modifications of the gas-liquid or liquid-liquid interface dynamics. As a result, EHD enjoys wide industrial applications in chemical engineering, e.g., coating processes, cooling systems of conducting fluids, electrospray technology, electrohydrodynamically enhanced heat transfer, etc. (the interested readers are referred to [1, 2] for a comprehensive overview). Due to the important role that EHD plays in the engineering community, an in-depth understanding of the mathematics behind the scene remains essential to the scientists working in this field. Early studies of this field can be traced back to the 1960s when Taylor & McEwan [3] first discovered that electric fields imposed in the normal direction to the surface could cause a destabilization to the flow. Later, Melcher & Schwarz [4] followed to study the same problem but with electric fields applied in the tangential direction, which showed the opposite effect. Based on linear stability analysis, it was found that the tangential electric field could provide a dispersive regularization on short waves. These two early works initiated research on EHD waves, and many results regarding flow stabilization/destabilization have been achieved ever since. For example, Barannyk *et al.* [5] developed a weakly nonlinear theory to demonstrate that the Rayleigh-Taylor instability can be suppressed by using horizontal electric fields. The results were examined and confirmed by direct numerical simulations in [6]. Solitary waves were even found in the Rayleigh-Taylor unstable regime under considerably strong horizontal electric fields in the full Euler equations by Guan & Wang [7]. On the other hand, horizontal electric fields were also shown by Zubarev & Kochurin [8] to be capable of suppressing the Kelvin-Helmholtz instability in the framework of reduced model equations.

Travelling waves propagating in two-dimensional space under the effects of gravity, surface tension, and electric field have been studied intensively by different authors, either with weakly nonlinear models or with the full Euler equations. The length scale of the present problem is at the capillary-gravity scale in centimeters or millimeters. The most general setup concerns two immiscible dielectric liquids of different depths, densities, and electric permittivities with a sharp free interface in between. Usually, additional assumptions were made to

simplify this complicated problem in previous works. For example, the problem was reduced to the one-layer case by assuming the upper layer to be a perfectly conducting gas as in [9, 10]; hence many analytical and numerical tools for handling the classical gravity-capillary wave problem can be generalized to the situation under investigation. Another assumption of practical relevance is to consider the lower fluid region as a conductor and the upper region as a dielectric gas. Despite this reduction, the full problem is still mathematically challenging due to its two-layered nature. Weakly nonlinear model equations were derived in the long-wave limits, e.g., the Korteweg-de Vries equation (KdV) and its variants [11] and the Benjamin equation [12]. A comprehensive work by [13] not only extended the long-wave models to three dimensions by using an approach of expanding the Dirichlet-Neumann operator (DNO) but also derived the nonlinear Schrödinger equation (NLS) for modulated wavetrains. A quintic truncation model was proposed in [14] based on the DNO expansion technique, and dark solitary waves, solitary wavepackets, and generalized solitary waves (with non-decaying trains of ripples in the far-field) were all found to exist in the vicinity of the phase speed minimum of the dispersion relation. Recently, Doak *et al.* [15] considered the general setup without any assumptions and summarized previous works using linear theories. Also, in the same paper, fully nonlinear computations were conducted for solitary waves and generalized solitary waves by a boundary integral equation method.

It is well known that the weakly nonlinear theory of wave interactions was pioneered by Phillips [16]. Phillips showed that resonant triads are impossible for surface gravity waves, but quartet interactions can occur at the cubic nonlinearity. In 1968, Zakharov derived the cubic NLS for gravity waves in [17], which is, in fact, a particular case of four-wave interactions (see the celebrated paper [18]) with

$$\underbrace{(k+\delta k)}_{k_1}+\underbrace{(k-\delta k)}_{k_2}-\underbrace{k}_{k_3}=\underbrace{k}_{k_4}\,,\quad \underbrace{(\omega+\delta\omega)}_{\omega_1}+\underbrace{(\omega-\delta\omega)}_{\omega_2}-\underbrace{\omega}_{\omega_3}=\underbrace{\omega}_{\omega_4}\,, \tag{1.1}$$

where k and ω represent wavenumber and angular frequency, respectively, while δk and $\delta\omega$ are detuning parameters. It is seen from (1.1) that a wave of wavenumber k and frequency ω can interact with the other two waves of nearly the same wavenumber and frequency subject to sideband perturbation. This particular quartet results in the cubic NLS for a single-mode wavetrain, which can be used to study sideband or modulational instabilities. Later, McGoldrick [19] continued to develop the general theory with the inclusion of surface tension by using a second-order analysis and found that three-wave interactions can

occur at the quadratic order. The work was extended by Simmons [20] via a variational approach and by Case & Chiu [21] via a perturbation analysis. McGoldrick followed by investigating the second harmonic resonance in [22], where the exact solutions in terms of elliptic functions were discovered in the case of wave amplitude varying slowly in space. Another important resonance, the so-called long-short wave interaction first pioneered by Benney [23], occurs among short waves and long waves when the long-wave speed matches the group speed of the short-wave envelope. It was discovered by Djordjevic & Redekopp [24] that the cubic NLS is invalid at the wavenumbers where the second harmonic resonance or the long-short wave interaction occurs since its nonlinear term becomes singular. It was also investigated in the case of a two-fluid system by Criag *et al.* [25] in which an envelop Schrödinger-type model was derived.

The general conditions for three-wave resonance in two dimensions are given by

$$k_1 \pm k_2 = \pm k_3 \,, \qquad \omega_1 \pm \omega_2 = \pm \omega_3 \,, \tag{1.2}$$

where k_j and ω_j $(j = 1, 2, 3)$ are the wavenumbers and frequencies, respectively. The second harmonic resonance and long-short wave interaction are, in fact, two special cases of triad resonances, which can be briefly summarized as follows.

- For the second harmonic resonance, whose associated wavenumber is denoted as k_s, the resonant conditions are

$$\underbrace{k_s}_{k_1} + \underbrace{k_s}_{k_2} = \underbrace{2k_s}_{k_3} \,, \qquad \underbrace{\omega(k_s)}_{\omega_1} + \underbrace{\omega(k_s)}_{\omega_2} = \underbrace{\omega(2k_s)}_{\omega_3} \,. \tag{1.3}$$

  It immediately implies that $c_p(k_s) = c_p(2k_s)$, where $c_p \coloneqq \frac{\omega(k)}{k}$ is the phase speed.

- For the long-short wave interaction, whose associated wavenumber is denoted as k_l, the resonant conditions are

$$\underbrace{(k_l + \delta k)}_{k_1} - \underbrace{\delta k}_{k_2} = \underbrace{k_l}_{k_3} \,, \qquad \underbrace{\omega(k_l + \delta k)}_{\omega_1} - \underbrace{\omega(k_l)}_{\omega_2} = \underbrace{\omega(\delta k)}_{\omega_3} \,. \tag{1.4}$$

  In the limit $\delta k \to 0$, the frequency condition reduces to $c_g(k_l) = c_0$, where $c_g \coloneqq \frac{\mathrm{d}\omega}{\mathrm{d}k}$ is the group speed and $c_0 \coloneqq c_p(0)$ is the long-wave speed.

In this work, we investigate the resonances mentioned above in the electrified Euler equation. To gain analytical insights, we first study the associated envelope equations analytically in the weakly nonlinear regime. These reduced

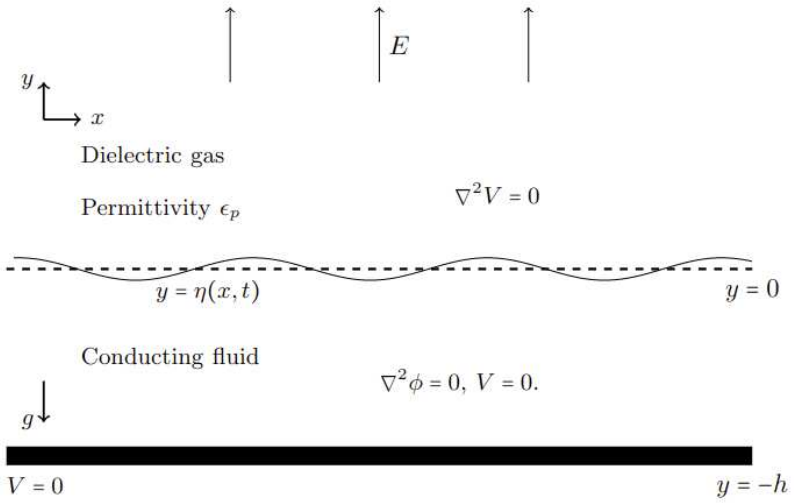

Figure 1: Schematic of the problem.

models, including the resonant triad, second harmonic resonance, long-short wave interaction, and NLS, are derived using the method of multiple scales. We also seek a connection between the NLS and resonances (1.3) and (1.4). We confine ourselves to the interface between a perfectly conducting liquid of finite depth and a dielectric gas of infinite depth under a normal electric field. A novel numerical scheme based on a time-dependent hodograph transformation (pioneered by Dyachenko *et al.* [26] for a one-layered fluid problem) coupled with an interpolation technique is introduced to conduct unsteady simulations of the full Euler equations, which have not been achieved in the literature to our knowledge.

The rest of the paper is structured as follows. The problem is mathematically formulated in §2. The weakly nonlinear envelope equations for resonant triads, long-short wave interactions, and a single-mode modulated wavetrain are derived in §3 using multi-scale analyses with various time and spatial scales. The numerical scheme for the fully nonlinear problem is proposed in §4, followed by the numerical simulations presented in §5. Finally, a conclusion is given in §6.

2. Modelling

We consider a two-dimensional inviscid, incompressible, and perfectly conducting fluid of constant density ρ and finite depth h bounded below by a flat electrode. We first introduce a Cartesian coordinate system with the horizontal coordinate x directed along the undisturbed free surface and a vertical coordinate y measured upwards from the equilibrium surface. The free-surface displacement is denoted by $y = \eta(x,t)$, a function varying with space and time. The flow is assumed to be irrotational, then the velocity field $\overrightarrow{u}$ for the fluid body can be represented by the gradient of a potential function ϕ, namely $\overrightarrow{u} = \nabla\phi$. The incompressibility condition, $\nabla \cdot \overrightarrow{u} = 0$, implies that the velocity potential satisfies the Laplace equation

$$\Delta\phi = 0\,, \qquad \text{for } -h < y < \eta(x,t)\,. \tag{2.1}$$

We assume that the fluid is perfectly conducting so that the electric strength is zero within the fluid. The surrounding medium, which occupies the region above the liquid, is assumed to be dielectric with permittivity ϵ_p. Its density is very small and negligible in comparison to that of the conducting fluid. The upper layer is of great depth and assumed to be infinitely long. An electric field acts along the positive y-direction with a uniform value E_0 in the far-field. The electrostatic limit of Maxwell's equation implies that the induced magnetic fields are negligible, and it then follows that the electric field is also irrotational due to Faraday's law. Therefore, we can introduce the voltage potential V, such that the electric field above the liquid surface, $\overrightarrow{E}$, satisfies $\overrightarrow{E} = \nabla V$, and hence the voltage potential satisfies

$$\Delta V = 0\,, \qquad \text{for } y > \eta(x,t)\,. \tag{2.2}$$

Due to the conducting nature of the fluid, the voltage potential V is invariant in the fluid domain and chosen to be 0 without losing generality. Then a boundary condition for V is imposed on the free surface:

$$V = 0\,, \qquad \text{on } y = \eta(x,t)\,. \tag{2.3}$$

A schematic is presented in Figure 1. The motion of the fluid satisfies the kinematic boundary conditions on the free surface and no penetration condition on the rigid bottom, namely

$$\eta_t = \phi_y - \eta_x\phi_x\,, \qquad \text{on } y = \eta(x,t)\,, \tag{2.4}$$

$$\phi_y = 0\,, \qquad \text{on } y = -h\,, \tag{2.5}$$

where the subscripts denote partial derivatives. Although the voltage potential vanishes on the free surface, the normal component of the electric field gives rise to normal stress. Therefore, the electric field and the fluid motion are coupled through the Maxwell stress tensor leading to the modified Bernoulli law at $y = \eta(x,t)$:

$$\phi_t + \frac{1}{2}|\nabla\phi|^2 + g\eta - \frac{\epsilon_p}{2\rho}|\nabla V|^2 - \frac{\sigma}{\rho}\frac{\eta_{xx}}{(1+\eta_x^2)^{3/2}} = 0\,, \tag{2.6}$$

where g is the acceleration due to gravity and σ is the coefficient of surface tension. Following [13], we introduce a new voltage potential $W = V/E_0 - y$, so that W is a harmonic function with

$$W_y \to 0\,, \qquad \text{as } y \to \infty\,, \tag{2.7}$$

$$W = -\eta\,, \qquad \text{on } y = \eta(x,t)\,. \tag{2.8}$$

We further non-dimensionalize the system by choosing h, $\sqrt{h/g}$, $E_0 h$ as reference length, time, and voltage potential, respectively. Therefore the Bernoulli equation can be rewritten as

$$\phi_t + \frac{1}{2}|\nabla\phi|^2 - \frac{E}{2}\left(|\nabla W|^2 + 2W_y\right) + \eta - \frac{B\eta_{xx}}{(1+\eta_x^2)^{3/2}} = 0\,, \tag{2.9}$$

where $E = \epsilon_p E_0^2/(\rho g h)$ is the electric Weber number and $B = \sigma/(\rho g h^2)$ is the Bond number, while the kinematic boundary conditions remain the same.

3. Nonlinear Envelope Equations

In this section, we focus on the weakly nonlinear theories of EHD wave interactions. Envelope equations will be derived for the general resonant triad, second harmonic resonance, long-short wave interaction, and modulation of a single-mode wavetrain. The purpose of the section is twofold: to provide theoretical underpinnings and initial conditions for wave interactions in the full Euler computations, and to understand nonlinear effects of the electric field on wave instabilities for some special cases.

3.1. Resonant triad interactions

This subsection develops a general theory for resonant three-wave interactions of electrocapillary-gravity waves by considering a single triad with k_j and ω_j $(j = 1,2,3)$ satisfying the resonant conditions (1.2). We select the plus sign

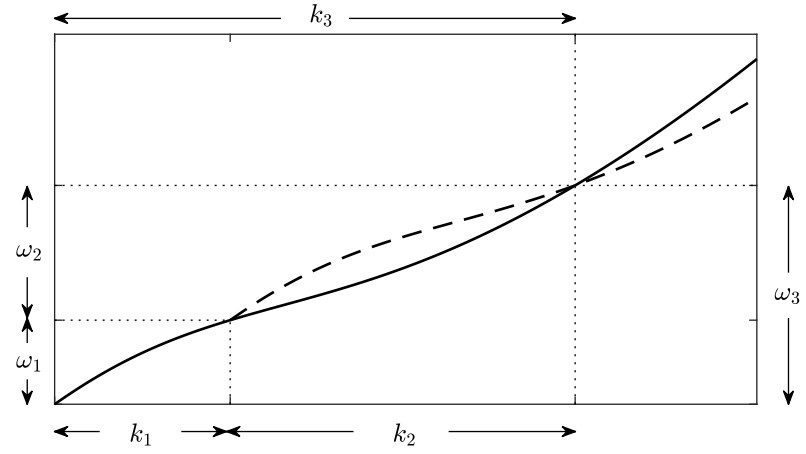

Figure 2: Angular frequency $\omega(k)$ (solid curve) and $\omega(k-k_1)+\omega_1$ (dashed curve). The resonant triad occurs at the intersection of the two curves. The plotting scale is exaggerated for a good display.

without loss of generality; therefore only the sum-type interactions are concerned, i.e.,

$$k_1 + k_2 = k_3\,, \qquad \omega_1 + \omega_2 = \omega_3\,, \tag{3.1}$$

as shown in the illustrating diagram in Figure 2.

We define slow variables $X = \epsilon x$ and $T = \epsilon t$, where ϵ is a small positive parameter that measures the wave steepness. In the case of weak nonlinearity, η and ϕ are assumed to be of order ϵ. The asymptotic solution can be written in the form:

$$\eta = \epsilon\left(A_{11}e^{\mathrm{i}\theta_1} + A_{12}e^{\mathrm{i}\theta_2} + A_{13}e^{\mathrm{i}\theta_3}\right) + \epsilon^2\left(A_{21}e^{\mathrm{i}\theta_1} + A_{22}e^{\mathrm{i}\theta_2} + A_{23}e^{\mathrm{i}\theta_3}\right) + \cdots + \text{c.c.}\,, \tag{3.2}$$

$$\phi = \epsilon\varphi_{10} + \epsilon\left(\phi_{11}e^{\mathrm{i}\theta_1} + \phi_{12}e^{\mathrm{i}\theta_2} + \phi_{13}e^{\mathrm{i}\theta_3}\right) + \epsilon^2\left(\phi_{21}e^{\mathrm{i}\theta_1} + \phi_{22}e^{\mathrm{i}\theta_2} + \phi_{23}e^{\mathrm{i}\theta_3}\right) + \cdots + \text{c.c.}\,, \tag{3.3}$$

$$\begin{aligned} W = &-\epsilon\left(A_{11}e^{\Theta_1} + A_{12}e^{\Theta_2} + A_{13}e^{\Theta_3}\right) - \epsilon^2\left(A_{21}e^{\Theta_1} + A_{22}e^{\Theta_2} + A_{23}e^{\Theta_3}\right) \\ &- \epsilon^2\left(\frac{\mathrm{i}k_1 y}{|k_1|}A_{11X} + |k_2|A_{13}A_{12}^* + |k_3|A_{13}A_{12}^*\right)e^{\Theta_1} \\ &- \epsilon^2\left(\frac{\mathrm{i}k_2 y}{|k_2|}A_{12X} + |k_1|A_{13}A_{11}^* + |k_3|A_{13}A_{11}^*\right)e^{\Theta_2} \\ &- \epsilon^2\left(\frac{\mathrm{i}k_3 y}{|k_3|}A_{13X} + |k_1|A_{11}A_{12} + |k_2|A_{11}A_{12}\right)e^{\Theta_3} + \cdots + \text{c.c.}\,, \end{aligned} \tag{3.4}$$

where 'c.c.' stands for complex conjugation, A_{ij} and φ_{ij} depend only on the slow variables X and T, $\phi_{1j} = \varphi_{1j}\cosh\left(k_j(y+1)\right)$, $\theta_j = k_j x - \omega_j t$, and $\Theta_j = \mathrm{i}\theta_j - |k_j| y$ (for $j = 1, 2, 3$). Substituting the ansatz (3.2)–(3.4) into (2.4) and (2.9) and collecting terms of different modes yield, to leading order, the linear dispersion relation

$$\omega^2 = k\left(1 - E|k| + Bk^2\right)\tanh k\,, \tag{3.5}$$

and the resonance equations (see also [18, 19, 20]) at quadratic order

$$\begin{cases} A_{11T} + \omega'(k_1)A_{11X} = \mathrm{i}\mu_1 A_{13}A_{12}^*\,, \\ A_{12T} + \omega'(k_2)A_{12X} = \mathrm{i}\mu_2 A_{13}A_{11}^*\,, \\ A_{13T} + \omega'(k_3)A_{13X} = \mathrm{i}\mu_2 A_{11}A_{12}\,, \end{cases} \tag{3.6}$$

where the coupling coefficients μ_j (by making use of (3.1) to derive the simplest form) are

$$\mu_j = \frac{k_j \tanh k_j}{2\omega_j}\left(2Ek_1k_2 + \omega_1^2 + \omega_2^2 + \omega_1\omega_2 - M\right)\,, \tag{3.7}$$

with $\omega_j \coloneqq \omega(k_j)$ for $j \in \{1, 2, 3\}$ and

$$M = \frac{\omega_2\omega_3}{\tanh k_2 \tanh k_3} + \frac{\omega_1\omega_3}{\tanh k_1 \tanh k_3} + \frac{\omega_1\omega_2}{\tanh k_1 \tanh k_2}\,. \tag{3.8}$$

When $E = 0$, the models (3.5)–(3.7) are reduced to the ones for capillary-gravity waves. In the particular case where the envelopes have no spatial variations in amplitude (i.e., A_{1j} are independent of X), (3.6) is reduced to three ordinary differential equations with exact solutions in terms of elliptic functions with periodic behaviour. The wave dynamics usually involve energy transfer between the three modes (see [19, 20]), a core feature of the solutions. It will be examined numerically with the fully nonlinear equations in §5.

The original three-wave resonance equations (3.6) have a rich structure as they form a Hamiltonian system that is integrable (see [27] and references therein). They can be solved analytically by the inverse scattering method for a broad class of initial conditions (see [28] for details). However, there is no general solution to (3.6) subject to arbitrary initial conditions. We can overcome this difficulty by computing the full Euler equations based on a scheme presented in §4.

3.1.1. Second harmonic resonance

The second harmonic resonance is a special case of three-wave interaction, as discussed in (1.3). It occurs when a wave of a specific wavenumber k_s propagates

at the identical speed of its second harmonic, i.e., $\omega(2k_s) = 2\omega(k_s)$, which gives rise to the Wilton ripples for capillary-gravity waves. However, it is not straightforward to derive the associated resonance equations directly from (3.6). For this case, a modified multi-scale analysis can be carried out under the same scaling as in section 3.1, based on the ansatz:

$$\eta = \epsilon A_{11} e^{\mathrm{i}\theta} + \epsilon A_{12} e^{2\mathrm{i}\theta} + \epsilon^2 A_{21} e^{\mathrm{i}\theta} + \epsilon^2 A_{22} e^{2\mathrm{i}\theta} + \cdots + \text{c.c.}\,, \tag{3.9}$$

$$\begin{aligned} W = &-\epsilon A_{11} e^{-|k|y} e^{\mathrm{i}\theta} - \epsilon A_{12} e^{-2|k|y} e^{2\mathrm{i}\theta} - \epsilon^2 \left(A_{21} + \frac{\mathrm{i}ky}{|k|} A_{11X} + 3|k| A_{11}^* A_{12} \right) e^{-|k|y} e^{\mathrm{i}\theta} \\ &- \epsilon^2 \left(A_{22} + \frac{\mathrm{i}ky}{|k|} A_{12X} + |k| A_{11}^2 \right) e^{-2|k|y} e^{2\mathrm{i}\theta} + \cdots + \text{c.c.}\,, \end{aligned} \tag{3.10}$$

and

$$\begin{aligned} \phi = &\epsilon\varphi_{10} + \epsilon\varphi_{11} \cosh(k(y+1)) e^{\mathrm{i}\theta} + \epsilon\varphi_{12} \cosh(2k(y+1)) e^{2\mathrm{i}\theta} \\ &+ \epsilon^2 \varphi_{20} + \epsilon^2 \Big[\varphi_{21} \cosh(k(y+1)) - \mathrm{i}(y+1) \sinh(k(y+1)) \varphi_{11X} \Big] e^{\mathrm{i}\theta} \\ &+ \epsilon^2 \Big[\varphi_{22} \cosh(2k(y+1)) - \mathrm{i}(y+1) \sinh(2k(y+1)) \varphi_{12X} \Big] e^{2\mathrm{i}\theta} + \cdots + \text{c.c.}\,, \end{aligned} \tag{3.11}$$

where $\theta = kx - \omega t$. We then substitute the above ansatz into the kinematic and dynamic boundary conditions. To $O(\epsilon)$, the solvability conditions for (A_{11}, φ_{11}) and (A_{12}, φ_{12}) yield

$$\begin{cases} \omega^2 = k \tanh k \left(1 - E|k| + Bk^2 \right), \\ 2\omega^2 = k \tanh(2k) \left(1 - 2E|k| + 4Bk^2 \right). \end{cases} \tag{3.12}$$

The solvability conditions for A_{21} and A_{22} at quadratic order give

$$\begin{cases} A_{11T} + \omega'(k) A_{11X} + \left(\omega^2 k \tanh k - \dfrac{3\omega^2 k}{\tanh k} + 2Ek^3 \tanh k \right) \dfrac{A_{11}^* A_{12}}{2\mathrm{i}\omega} = 0\,, \\ A_{12T} + \omega'(2k) A_{12X} + \left[k \tanh(2k) \left(\omega^2 - \dfrac{\omega^2}{2\sinh^2 k} + Ek^2 \right) - \dfrac{2\omega^2 k}{\tanh k} \right] \dfrac{A_{11}^2}{2\mathrm{i}\omega} = 0\,. \end{cases} \tag{3.13}$$

It is noted that the multi-scale analysis can be extended to the cubic order $O(\epsilon^3)$, where two more equations including A_{11}, A_{12}, A_{21}, and A_{22} can be derived (see [29]). Together with (3.13), one may obtain a system of four nonlinear partial differential equations with four unknowns, which was used by Jones [29] to demonstrate that the instability in this resonant case consistently shows up when the modulational wavenumber is sufficiently small. However, such equations are impractical for further analyses or computations due to the complicated

structure. Hence, the detail is omitted, and the numerical calculations will be achieved in the framework of the full Euler equations.

3.1.2. Long-short wave interactions

Interactions among short and long waves occur in a fluid of finite depth when the group speed c_g of the short-wave envelope matches the phase speed of the long wave, where the wavenumber for the short wave satisfies $c_g = 1$ under the present scaling. Although this interaction is also a special case of three-wave resonance, as discussed in (1.4), a different scaling is required since one of the resonant wavenumbers tends to zero. Following [24], we define $X = \epsilon^{2/3}x$, $T = \epsilon^{2/3}t$, and $\tau = \epsilon^{4/3}t$ and expand $\phi(X - c_gT, \tau, y)$ and $\eta(X - c_gT, \tau)$ as

$$\phi = \epsilon^{2/3}\varphi + \epsilon\phi_3 + \epsilon^{4/3}\phi_4 + \epsilon^{5/3}\phi_5 + \epsilon^2\phi_6 + \epsilon^{7/3}\phi_7 + \epsilon^{8/3}\phi_8 + \cdots, \tag{3.14}$$

$$\eta = \epsilon Ae^{\mathrm{i}\theta} + \epsilon^{4/3}A_4 + \epsilon^{5/3}A_5 + \epsilon^2A_6 + \epsilon^{7/3}A_7 + \epsilon^{8/3}A_8 + \cdots, \tag{3.15}$$

where, to leading order, A is the short-wave envelope and φ is the long-wave velocity potential. The functions A_j and ϕ_j, containing all Fourier modes, depend on $X - c_gT$, τ, and y. Their explicit forms can be found by solving the Laplace equation (2.1) together with the boundary conditions (2.4) and (2.5). It is readily shown that W can be expressed as

$$\begin{aligned} W = &-\epsilon Ae^{-|k|y}e^{\mathrm{i}\theta} - \epsilon^{4/3}\left(A_{40} + A_{41}e^{-|k|y}e^{\mathrm{i}\theta}\right) - \epsilon^{5/3}\Big(A_{50} + A_{51}e^{-|k|y}e^{\mathrm{i}\theta} \\ &+ \frac{\mathrm{i}ky}{|k|}e^{-|k|y}A_Xe^{\mathrm{i}\theta}\Big) - \epsilon^2\left(A_{60} + 2|k||A|^2 + A_{61}e^{-|k|y}e^{\mathrm{i}\theta} + \frac{\mathrm{i}ky}{|k|}e^{-|k|y}A_{41X}e^{\mathrm{i}\theta}\right) \\ &- \epsilon^{7/3}\Big[A_{70} + 2|k|\left(AA_{41}^* + A^*A_{41}\right) + \left(A_{71} + |k|AA_{40}\right)e^{-|k|y}e^{\mathrm{i}\theta} \\ &+ \frac{\mathrm{i}ky}{|k|}e^{-|k|y}A_{51X}e^{\mathrm{i}\theta} - \frac{y^2}{2}e^{-|k|y}A_{XX}e^{\mathrm{i}\theta}\Big] + \cdots + \text{c.c.}\,. \end{aligned} \tag{3.16}$$

We then substitute these expressions into the kinematic and dynamic boundary conditions and equate terms like the power of ϵ. By performing similar calculations to those in [24], a model equation is discovered by collecting the coefficients of $\epsilon^{8/3}e^{i\theta}$, which is of the form

$$\mathrm{i}A_\tau + \lambda A_{XX} = \alpha A\varphi_X\,, \tag{3.17}$$

where

$$\lambda = \frac{\omega''(k)}{2}\,, \quad \alpha = \frac{1}{2\omega}\left(2\omega k + \frac{\omega^2 k c_g}{\sinh k\,\cosh k}\right). \tag{3.18}$$

The zeroth mode of $O\left(\epsilon^{8/3}\right)$ in the kinematic boundary condition gives

$$\left(\varphi_X\right)_\tau = -\left(\frac{\omega^2}{2\sinh^2 k} + \frac{\omega}{\tanh k\, c_g}\right)\left(|A|^2\right)_X\,. \tag{3.19}$$

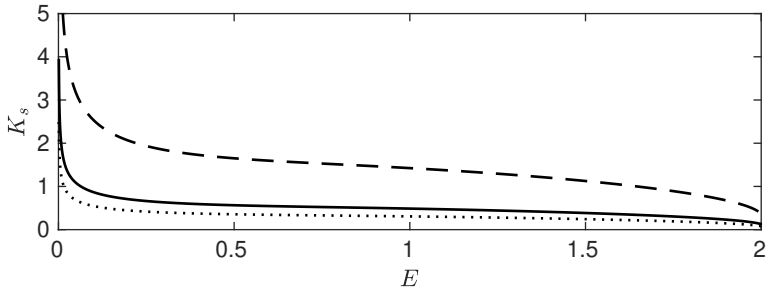

Figure 3: The modulational wavenumber K_s versus E for $B = 1$ when $\max|A| = 0.1$ (solid), $\max|A| = 0.05$ (dotted) and $\max|A| = 0.5$ (dashed).

Then (3.17) and (3.19) together form a system of two coupled equations which were used by Djordjevic & Redekopp [24] for the stability analysis. It was shown that the instability appears when

$$K < K_s = \sqrt{3}\left(\frac{\Delta|A|^2}{\lambda^2}\right)^{\frac{1}{3}}, \tag{3.20}$$

where K is the modulational wavenumber and

$$\Delta = \alpha\left(\frac{\omega^2}{2\sinh^2 k} + \frac{\omega}{\tanh k\, c_g}\right). \tag{3.21}$$

Such a result is similar to the one discovered for the second harmonic resonance, where the instability appears provided the modulational wavenumber is sufficiently small. As shown in Figure 3, the threshold value K_s for a fixed amplitude decreases as the strength of the electric field increases. In other words, the electric field from a weakly nonlinear viewpoint has the effect of suppressing the instability subject to finite wavelength perturbations since the range of unstable wavenumbers shrinks as the strength of the electric field increases. On the other hand, a wave of larger amplitude is more easily destabilized by a fixed electric field.

3.2. NLS – a special case of quartet resonance

For a weakly nonlinear wavetrain, we can assume η, ϕ, and W are of order ϵ, where ϵ is a small positive parameter that measures the wave slope. It follows that the velocity potential and voltage potential on the free surface can be expanded about $y = 0$ as

$$\phi(x,\eta,t) = \phi(x,0,t) + \eta\phi_y(x,0,t) + \frac{\eta^2}{2}\phi_{yy}(x,0,t) + O\left(\epsilon^4\right), \tag{3.22}$$

$$W(x,\eta,t) = W(x,0,t) + \eta W_y(x,0,t) + \frac{\eta^2}{2} W_{yy}(x,0,t) + O\left(\epsilon^4\right) . \tag{3.23}$$

Expanding the boundary conditions (2.4), (2.8), and (2.9) about $y = 0$ yields

$$\eta_t - \phi_y = \eta\phi_{yy} - \eta_x\phi_x + \frac{\eta^2}{2}\phi_{yyy} - \eta\eta_x\phi_{xy} , \tag{3.24}$$

$$\begin{aligned} \phi_t + \eta - B\eta_{xx} - EW_y = & -\eta\phi_{ty} - \frac{1}{2}\left(\phi_x^2 + \phi_y^2\right) + \frac{E}{2}\left(W_x^2 + W_y^2 + 2\eta W_{yy}\right) \\ & - \frac{\eta^2}{2}\phi_{tyy} - \eta\phi_x\phi_{xy} - \eta\phi_y\phi_{yy} - \frac{3}{2}B\eta_x^2\eta_{xx} \\ & + \frac{E}{2}\left(2\eta W_x W_{xy} + 2\eta W_y W_{yy} + \eta^2 W_{yyy}\right) , \end{aligned} \tag{3.25}$$

and

$$W + \eta = -\eta W_y - \frac{\eta^2}{2} W_{yy} , \tag{3.26}$$

where nonlinear terms are retained up to cubic order, and all variables are evaluated at $y = 0$. We consider a quasi-monochromatic wave propagating with the group speed c_g and oscillating fast in the x-direction. The slow variables are denoted as $X = \epsilon x$, $T = \epsilon t$, $\tau = \epsilon^2 t$, and $e^{\mathrm{i}(kx-\omega t)}$ is chosen to be the carrier wave. Following [24], we seek an asymptotic solution of these equations in the form

$$\begin{aligned} \phi = & \epsilon\varphi + \epsilon\varphi_{11}\cosh(k(y+1))e^{\mathrm{i}\theta} + \epsilon^2\varphi_{20} + \epsilon^2\varphi_{21}\cosh(k(y+1))e^{\mathrm{i}\theta} \\ & - \mathrm{i}\epsilon^2(y+1)\sinh(k(y+1))\varphi_{11X}e^{\mathrm{i}\theta} + \epsilon^2\varphi_{22}\cosh(2k(y+1))e^{2\mathrm{i}\theta} \\ & + \epsilon^3\varphi_{30} - \frac{\epsilon^3}{2}(y+1)^2\varphi_{XX} - \mathrm{i}\epsilon^3(y+1)\sinh(k(y+1))\varphi_{21X}e^{\mathrm{i}\theta} \\ & - \frac{\epsilon^3}{2}(y+1)^2\cosh(k(y+1))\varphi_{11XX}e^{\mathrm{i}\theta} + \epsilon^3\varphi_{31}\cosh(k(y+1))e^{\mathrm{i}\theta} + \cdots + \text{c.c.} , \end{aligned} \tag{3.27}$$

$$\eta = \epsilon A e^{\mathrm{i}\theta} + \epsilon^2\left(A_{20} + A_{21}e^{\mathrm{i}\theta} + A_{22}e^{2\mathrm{i}\theta}\right) + \epsilon^3\left(A_{30} + A_{31}e^{\mathrm{i}\theta}\right) + \cdots + \text{c.c.} , \tag{3.28}$$

and

$$\begin{aligned} W = & -\epsilon A e^{-|k|y}e^{\mathrm{i}\theta} - \epsilon^2\Big[\left(A_{20} + 2|k||A|^2\right) + \left(A_{21} + \frac{\mathrm{i}ky}{|k|}A_X\right)e^{-|k|y}e^{\mathrm{i}\theta} \\ & + \left(A_{22} + |k|A^2\right)e^{-2|k|y}e^{2\mathrm{i}\theta}\Big] - \epsilon^3\Big[A_{31} + 2|k|A_{22}A^* + |k|A_{20}A \\ & + \frac{1}{2}k^2|A|^2A + \frac{\mathrm{i}ky}{|k|}A_{21X} - \frac{1}{2}y^2A_{XX}\Big]e^{-|k|y}e^{\mathrm{i}\theta} + \cdots + \text{c.c.} , \end{aligned} \tag{3.29}$$

where A_{ij} and φ_{ij} depend only on the slow variables $X - c_gT$ and τ. A and φ have been used to replace A_{11} and φ_{10}, respectively, for easy notations. Here

c_g is the speed of the envelope by definition. We substitute the above solutions into the kinematic and dynamic boundary conditions on the free surface. The solvability condition for (A, φ_{11}) obtained at $O(\epsilon)$ yields the linear dispersion relation (3.5).

To quadratic order, collecting the coefficients of $\epsilon^2 e^{\mathrm{i}\theta}$ yields a system of two equations for unknowns A_{21} and φ_{21}, which is solvable only if the following condition is satisfied:

$$c_g = \frac{\left(1 - 2E|k| + 3Bk^2\right)\tanh k}{2\omega} + \omega\,\mathrm{csch}(2k)\,. \tag{3.30}$$

The right-hand side of (3.30) is the derivative of ω with respect to k, denoted by $\omega'(k)$ or the group speed of the wave. Next, a solvability condition for A_{31} and φ_{31} is found by collecting the terms in $\epsilon^3 e^{\mathrm{i}\theta}$. A further simplification by eliminating all the variables from the quadratic order, such as A_{20} and A_{22}, using the equalities obtained for the zeroth and second modes at $O(\epsilon^2)$ yields a reduce equation for wave envelope (the so-called cubic nonlinear Schrödinger equation) as follows

$$\mathrm{i}A_\tau + \lambda A_{XX} + \delta|A|^2 A = 0 \tag{3.31}$$

with

$$\lambda = \frac{\omega''(k)}{2}\,, \qquad \delta = \frac{\alpha_1 + \alpha_2 + \alpha_3 + \alpha_4}{2\omega}\,, \tag{3.32}$$

where

$$\alpha_1 = \frac{2\omega k}{1 - c_g^2}\left(1 + \frac{\omega c_g}{\sinh 2k}\right)\left(\frac{\omega^2 c_g}{\sinh^2 k} + \frac{2\omega}{\tanh k}\right), \tag{3.33}$$

$$\alpha_2 = k^3\left(Ek^2 - \frac{\omega^2}{\sinh^2 k}\right)\frac{\left(\tanh^2 k - 3\right)\left(1 - E|k| + Bk^2\right) + 2Ek\tanh k}{\left(\omega_2^2 - 4\omega^2\right)\coth(2k)}\,, \tag{3.34}$$

$$\alpha_3 = \frac{2\omega^2 k^2\left[\left(3 - 5E|k| + 9Bk^2\right)k - \tanh k\left(3\omega^2 + 2Ek^2\right)\right]}{\left(\omega_2^2 - 4\omega^2\right)\coth(2k)\tanh^2 k}\,, \tag{3.35}$$

$$\alpha_4 = \frac{2\omega^4 k}{\sinh(2k)\sinh^2 k} + k^3\tanh k\left(-4 + 2E|k| - \tfrac{5}{2}Bk^2\right), \tag{3.36}$$

and $\omega_2 := \omega(2k)$. As shown in Figure 4, two asymptotic lines exist at $k = k_s$ and $k = k_l$ in the graph of δ versus k, corresponding to singularities in the coefficients caused by the second harmonic and long-short wave resonances, respectively. It is noted that such an argument is also valid for the capillary-gravity wave problem in the presence of constant vorticity, as investigated in [30]. Interesting features have been observed when the two singularities take place and are to be discussed in detail as follows.

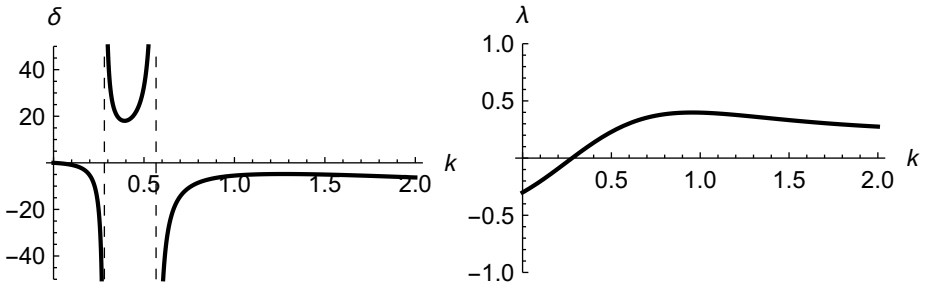

Figure 4: The values of δ and λ for $E = 0.6$ and $B = 1$ versus the wavenumber k. There are two asymptotes (vertical dashed lines) in the $k - \delta$ figure at $k = k_s$ (left) and $k = k_l$ (right).

1. When $\omega_2^2 = 4\omega^2$, the coefficients α_2 and α_3 become singular. This case corresponds to the second harmonic resonance when a wave and its second harmonic propagate at the same speed. From a wave-resonance perspective, the four-wave resonant conditions (1.2) reduce to

$$\underbrace{(k_s + \delta k)}_{k_1} + \underbrace{(k_s - \delta k)}_{k_2} = \underbrace{k_s + k_s}_{k_{3,4}}, \tag{3.37}$$

$$\underbrace{(\omega + \delta\omega)|_{k=k_s}}_{\omega_1} + \underbrace{(\omega - \delta\omega)|_{k=k_s}}_{\omega_2} = \underbrace{\omega(2k_s)}_{\omega_{3,4}}, \tag{3.38}$$

where we have used the identity $\omega(k_s) + \omega(k_s) = \omega(2k_s)$.

2. When $c_g^2 = 1$, the coefficient α_1 turns out to be singular. This situation is consistent with the long-short wave interaction when the envelope speed of a wave matches the long wave speed (which is equal to 1 under our scaling). The four-wave resonant conditions (1.2) reduce to

$$\underbrace{(k_l + \delta k)}_{k_1} + \underbrace{(k_l - \delta k - k_l)}_{k_{2,3}} = \underbrace{k_l}_{k_4}, \tag{3.39}$$

$$\underbrace{(\omega + \delta\omega)|_{k=k_l}}_{\omega_1} - \underbrace{\omega(\delta k)}_{\omega_{2,3}} = \underbrace{\omega(k_l)}_{\omega_4}, \tag{3.40}$$

where we have used $(\omega - \delta\omega - \omega)|_{k=k_l} = -\delta\omega|_{k=k_l} = -\omega(\delta k)$ in the limit $\delta k \to 0$.

In the above two exceptional cases, two resonant wave modes are merged into one at the specific wavenumbers, resulting in a transition from a four-wave resonance to a three-wave resonance. This leads to a breakdown of the original scaling, which causes δ from the NLS (3.31) to be singular. It is worth

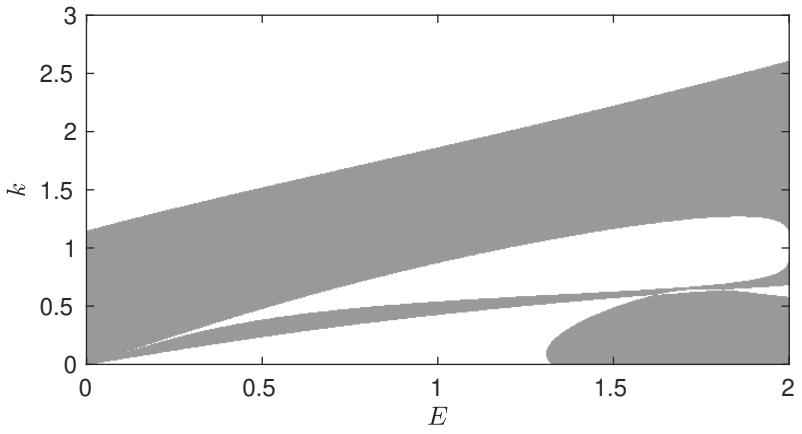

Figure 5: The NLS type for different value of E and k when $B = 1$. The white regions correspond to the defocusing NLS regime predicting modulational stability. The grey regions show the other way around.

mentioning that such an argument remains valid for other problems with similar dispersion relations, such as flexural-gravity waves. Further investigations of nonlinear wave interactions will be conducted numerically by an improved time-dependent conformal mapping scheme introduced in the next section.

The vertical electric field can substantially impact the modulational instability since the coefficients λ and δ from (3.31) may change sign due to the presence of the electric terms in δ, causing a swap of the NLS type as can be seen in Figure 5. In the particular case of deep water as studied in [13, 14], at the phase speed minimum between two asymptotes, $k = k_s$ and $k = k_l$, the NLS type can be changed from being focusing to defocusing with a strong electric field, resulting in modulational stability of wavetrains and bifurcation of dark solitary waves.

4. Numerical scheme

This section presents a numerical scheme for the fully nonlinear problem (2.1)-(2.9), which can be regarded as an extension of the traditional hodograph transformation method pioneered by Dyachenko *et al.* [26]. Two time-dependent conformal mappings, f_1 and f_2, are introduced to facilitate solving the Laplace equations. They transform the fluid domain $-1 < y < \eta(x,t)$ and above region $y > \eta(x,t)$ onto a strip of finite depth D in the lower-half plane and the upper half plane, respectively (see Figure 6). The coordinates of the

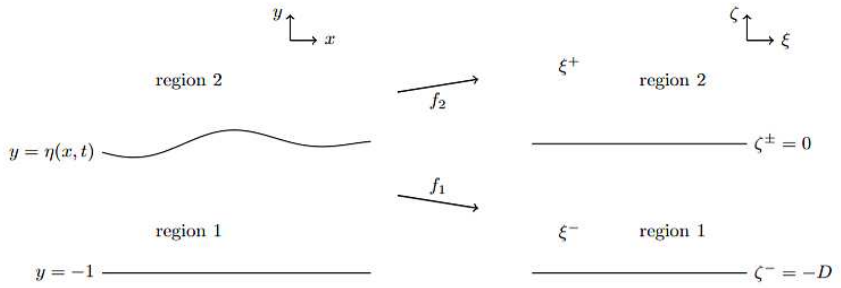

Figure 6: Schematic of the conformal mapping.

mapped plane are denoted by (ξ, ζ); thus, the free surface $y = \eta(x,t)$ mapped onto $\zeta = 0$ is now flattened. The canonical variables (ξ, ζ) in the upper layer are denoted by (ξ^+, ζ^+) and in the lower layer by (ξ^-, ζ^-). In the mapped plane, we defined spatial variables on the surface as $X^\pm = X(\xi^\pm, t) = x(\xi^\pm, 0, t)$ and $Y^\pm = Y(\xi^\pm, t) = y(\xi^\pm, 0, t)$. f_1 can be found by solving the boundary value problem

$$\Delta^- y = 0\,, \qquad \zeta^- < 0\,, \tag{4.1}$$

$$y = Y^-\,, \qquad \zeta^- = 0\,, \tag{4.2}$$

$$y = -1\,, \qquad \zeta^- = -D\,, \tag{4.3}$$

and similarly, for f_2, we need to solve

$$\Delta^+ y = 0\,, \qquad \zeta^+ > 0\,, \tag{4.4}$$

$$y = Y^+\,, \qquad \zeta^+ = 0\,, \tag{4.5}$$

$$y \sim \zeta^+\,, \qquad \zeta^+ \to \infty\,, \tag{4.6}$$

where $\Delta^\pm = \partial^2_{\xi^\pm} + \partial^2_{\zeta^\pm}$. For ease of notations, all the '$-$' superscripts are dropped. After some algebra, we obtain two relations on the surface

$$X = \xi - \mathcal{T}[Y]\,, \tag{4.7}$$

$$X^+ = \xi^+ + \mathcal{H}[Y^+]\,, \tag{4.8}$$

with $\mathcal{H}[.]$ and $\mathcal{T}[.]$ defined as

$$\mathcal{H}[g](\xi) = \frac{1}{\pi}\,\mathrm{PV}\int_{-\infty}^{\infty} \frac{g(\xi')}{\xi' - \xi}\,\mathrm{d}\xi'\,, \tag{4.9}$$

$$\mathcal{T}[g](\xi) = \frac{1}{2D}\,\mathrm{PV}\int_{-\infty}^{\infty} g(\xi')\coth\left[\frac{\pi}{2D}(\xi'-\xi)\right]\mathrm{d}\xi'\,, \tag{4.10}$$

where 'PV' means the integrals are in the Cauchy principal sense. The harmonic conjugates of $\phi(\xi,\zeta)$ and $v(\xi^+,\zeta^+)$, denoted by $\psi(\xi,\zeta)$ and $\nu(\xi^+,\zeta^+)$, respectively, are introduced. On the free surface, we define $\Phi(\xi,t) = \phi(\xi,0,t)$, $\Psi(\xi,t) = \psi(\xi,0,t)$, $V(\xi^+,t) = v(\xi^+,0,t)$, and $\Upsilon(\xi^+,t) = \nu(\xi^+,0,t)$. By solving the Laplace equations in region 1 for ϕ and in region 2 for v, one obtains

$$\Psi_\xi = \mathcal{T}[\Phi_\xi]\,, \tag{4.11}$$

$$\Upsilon_{\xi^+} = -1 - \mathcal{H}[V_{\xi^+}]\,. \tag{4.12}$$

We note that V_{ξ^+} is constantly zero due to condition (2.3). The time evolution equations for the surface displacement and surface velocity potential in the transformed plane are given by

$$Y_t = Y_\xi\mathcal{T}\left[\frac{\Psi_\xi}{J}\right] - X_\xi\frac{\Psi_\xi}{J}\,, \tag{4.13}$$

$$\Phi_t = \frac{1}{2J}\left(\Psi_\xi^2 - \Phi_\xi^2\right) - Y + T\kappa + \Phi_\xi\mathcal{T}\left[\frac{\Psi_\xi}{J}\right] + \frac{E}{2J^+}\,, \tag{4.14}$$

where $\kappa = (X_\xi Y_{\xi\xi} - Y_\xi X_{\xi\xi})J^{-3/2}$, $J = X_\xi^2 + Y_\xi^2$, and $J^+ = \left(X_{\xi^+}^+\right)^2 + \left(Y_{\xi^+}^+\right)^2$. The only ξ^+-dependent part is the electric term $E/2J^+$, which motivates us to use ξ as the primary variable. Thus, we propose a numerical scheme as follows: the wave dynamics are obtained by stepping the time-evolution equations (4.13) and (4.14) for (X,Y), as well as (4.13) for (X^+,Y^+) by making use of a spline interpolation technique. In particular, for travelling waves with a constant speed c, after some similar calculations, as shown in [31], we obtain a single integro-differential equation

$$\frac{c^2}{2}\left(\frac{1}{J}-1\right) + Y - T\kappa - \frac{E}{2}\left(\frac{1}{J^+}-1\right) = Be\,, \tag{4.15}$$

where Be is called the Bernoulli constant and is treated as an unknown (see [32] for a review). For periodic waves that are symmetric by $\xi = 0$, the surface elevation can be expressed using the Fourier series,

$$Y(\xi) = \sum_{n=1}^{N} a_n\cos\left(\frac{2n\pi\xi}{L}\right)\,,\quad Y^+(\xi^+) = \sum_{n=1}^{N} b_n\cos\left(\frac{2n\pi\xi^+}{L}\right)\,, \tag{4.16}$$

where the Fourier coefficients a_n and b_n are the unknowns, and the series are truncated after N terms. We introduce N collocation points uniformly distributed in a finite interval $[-L/2, L/2)$ along ξ and ξ^+

$$\xi_m = \xi_m^+ = \frac{(m-1)L}{N} - \frac{L}{2}\,,\qquad m = 1,2,...,N\,, \tag{4.17}$$

where L is the length of the computational domain. The fluid depth in the canonical plane is evaluated by

$$D = 1 + \frac{1}{L}\int_{-L/2}^{L/2} Y(\xi, t)\,\mathrm{d}\xi\,. \tag{4.18}$$

The wave amplitude A can be defined as

$$A = \frac{\max Y - \min Y}{2}\,. \tag{4.19}$$

The $\mathcal{T}$-transform and the Hilbert transform can be numerically computed with the aid of their Fourier symbols; namely,

$$\mathcal{T}[g] = \mathcal{F}^{-1}\Big[\coth(kD)\mathcal{F}[g]\Big], \quad \text{for } k \neq 0\,, \tag{4.20}$$

$$\mathcal{H}[g] = \mathcal{F}^{-1}\Big[\mathrm{i}\,\mathrm{sgn}(k)\mathcal{F}[g]\Big], \quad \text{for } k \neq 0\,, \tag{4.21}$$

where $\mathcal{F}$ stands for the Fourier operator and $\mathcal{F}^{-1}$ is its inverse. Both operators are identically 0 at $k = 0$. In our numerical experiments, $N = 2048$ is usually used. No significant change in the numerical results if N is further increased. We also fix the parameters $E = 0.6$ and $B = 1$. Qualitatively similar results are obtained for other finite values of E and B in the stable regime. The dynamic boundary condition (4.15) is satisfied at the grid points as defined in (4.17). Since the force term due to the electric fields from (4.15) is in $J^+(X^+, Y^+)$, a spline interpolation technique is used to transform data between (X, Y) and (X^+, Y^+). It yields $2N$ equations used to solve for the unknown coefficients a_n and b_n via Newton's method. The l^∞-norm residual errors are set to be less than 10^{-10} for the solutions to be considered converged. For unsteady simulations, a fourth-order Runge-Kutta method is employed for the time integration. The step size dt is chosen to be sufficiently small for numerical stability.

5. Numerical Results

We begin with computing travelling-wave solutions using the numerical scheme presented in section 4 to examine the overall performance of the interpolation technique. A number of examples are presented in Figure 7 for a small amplitude $A = 0.02$ and Figure 8 for a large amplitude $A = 0.45$, where (X, Y) and (X^+, Y^+) are both sketched. It is observed that higher nonlinearity broadens the waves, and such a phenomenon is mainly due to the capillary effect. Also, the graphs of (X, Y) agree very well with those of (X^+, Y^+).

To quantify and examine the accuracy of the fit of the two data sets, we introduce an overlap test for (X, Y) and (X^+, Y^+) that measures the mean

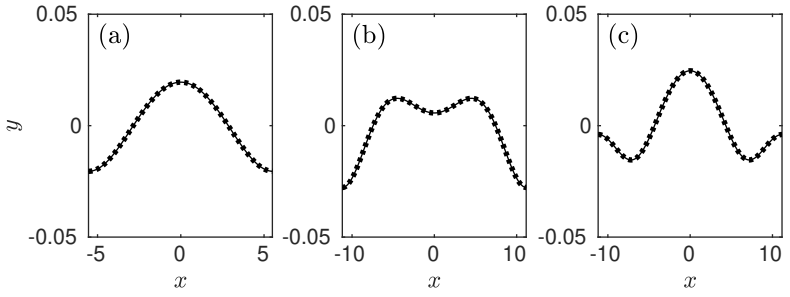

Figure 7: Typical wave profiles with $A = 0.02$ plotted in the physical plane. The solid curves are for (X, Y), and the dotted curves are for (X^+, Y^+). (a) A monochromatic wave with $k = k_l = 0.5668$. (b) A Wilton-Ripples type solution with $k = k_s = 0.2810$ and negative curvature at the wave center. (c) A Wilton-Ripples type solution with $k = k_s$ and positive curvature at the wave center.

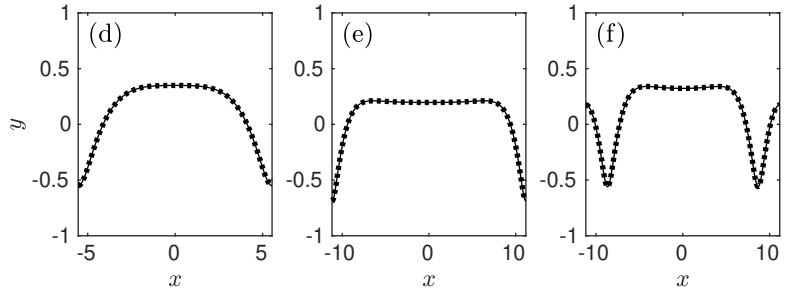

Figure 8: Same as Figure 7 but with a larger amplitude $A = 0.45$.

	(a)	(b)	(c)
$\bar{d}$	4.29×10^{-14}	3.99×10^{-10}	2.39×10^{-10}
	(d)	(e)	(f)
$\bar{d}$	6.46×10^{-9}	8.28×10^{-7}	4.27×10^{-8}

Table 1: The values of $\bar{d}$ for solution (a)-(f) as presented in Figures 7 and 8.

distance, denoted by $\bar{d}$, from points (X^+, Y^+) to the curve fitted by (X, Y). The corresponding values for solutions (a)-(f) are displayed in Table 1. As can be seen in the top panel for the case of weak nonlinearity, (X, Y) and (X^+, Y^+) match well because the $\bar{d}$-value is close to the numerical tolerance from Newton's method. Although the results become less impressive for high nonlinearity, as shown in the lower panel of Table 1, since the interpolation technique produces relatively significant errors under such circumstances, they remain at a satisfactory level. This overlap test is conducted throughout the subsequent numerical simulations to monitor the computational accuracy.

Next, we validate the time-dependent numerical scheme by conducting relatively simple numerical experiments of three-wave interactions involving energy transfer among the resonant modes. The following two settings are chosen.

1. $k_1 = k_2 = \frac{1}{2}k_3 = k_s$ $(= 0.2810)$, $L = 2\pi/k_s$, $N = 512$, $dt = 0.005$, and

$$\eta(x, 0) = 0.01 \cos(k_s x) \,. \tag{5.1}$$

2. $k_1 = \frac{1}{2}k_2 = \frac{1}{3}k_3 = k_*$ $(= 0.1865)$, $L = 2\pi/k_*$, $N = 512$, $dt = 0.0025$, and

$$\eta(x, 0) = 0.005 \cos(2k_* x) + 0.005 \cos(3k_* x) \,. \tag{5.2}$$

The initial inputs of Y^+ are obtained numerically by a fixed point iteration method. Following [22, 27], the resonance model equations (3.6) and (3.13) both admit exact solutions in terms of elliptic Jacobian functions subject to appropriate initial conditions. The predictions by the resonance models are presented together with the numerical simulations for the full Euler equations in Figures 9–12. The models can capture the main features of the resonances; that is, energy exchange takes place and oscillates periodically between the triad modes in the experiments. However, they cannot illustrate all the details, such as the maximum of a_2 from Figure 9 and the jittery curves of a_1 and a_2 from Figure 11.

A number of snapshots are depicted in Figures 10 and 12 for (X, Y) and (X^+, Y^+). Great accuracy has been achieved, with the $\bar{d}$-value from the overlap test always at the order of 10^{-10}. Overall, the time-dependent numerical

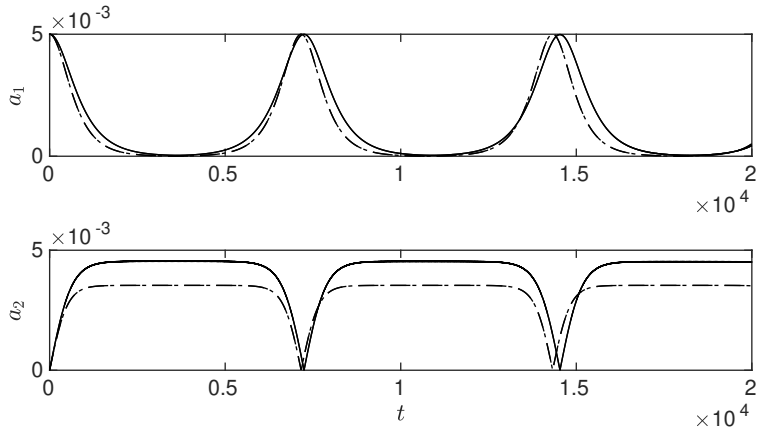

Figure 9: Experiment 1: the first two Fourier modes versus time t computed by the full Euler equations (solid curves) and predicted by the resonance equations (3.13) (dashed-dotted curves).

scheme based on two sets of collocation points and an interpolation approach has achieved excellent performance and is ready to tackle more nonlinear dynamics.

We move on to perform time-dependent computations for more complicated situations, where all Fourier modes are involved, by the numerical scheme introduced previously in §4. The modulational instability of wavetrains is to be examined with the following initial condition, as presented in [33],

$$\eta(x,0) = \left[1 + a\cos\left(Kx\right)\right]\eta_0(x)\,, \tag{5.3}$$

where η_0 is a periodic solution to the electrified Euler equations and $a\cos(Kx)$ is the modulational perturbation with a being a small real number. The modulational wavenumber K is selected to be k/n in which k is the carrier wavenumber, and n is a positive integer, or in other words, n carrier waves in a single modulation envelope. Only one modulation is considered in the domain, i.e. $K = 2\pi/L$. It is also noted that the initial disturbance (5.3) is imposed on both (X, Y) and (X^+, Y^+). To begin with, we consider two examples for the case of a single wavetrain:

3. $k = 1$, $K = k/16 = 0.0625$, $L = 100.5310$, $a = 0.05$, $N = 4096$, and $dt = 0.002$ (the associated NLS is of defocusing type);

4. $k = 0.5$, $K = k/16 = 0.03125$, $L = 200.0619$, $a = 0.05$, $N = 4096$, and $dt = 0.001$ (the associated NLS is of focusing type).

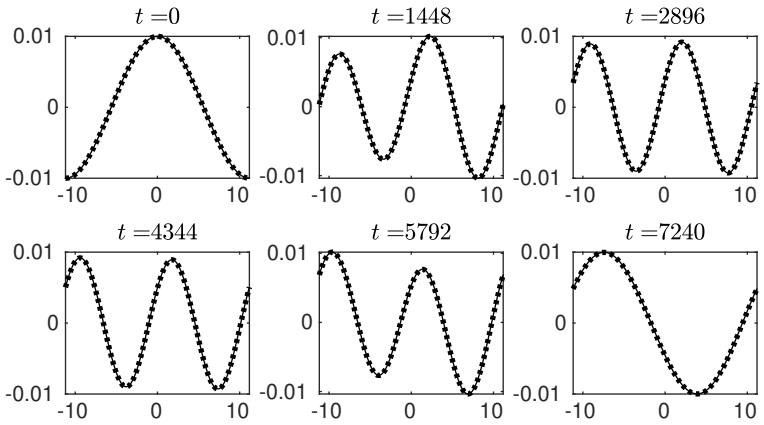

Figure 10: Experiment 1: snapshots of wave profiles of (X, Y) (solid curves) and (X^+, Y^+) (dotted curves).

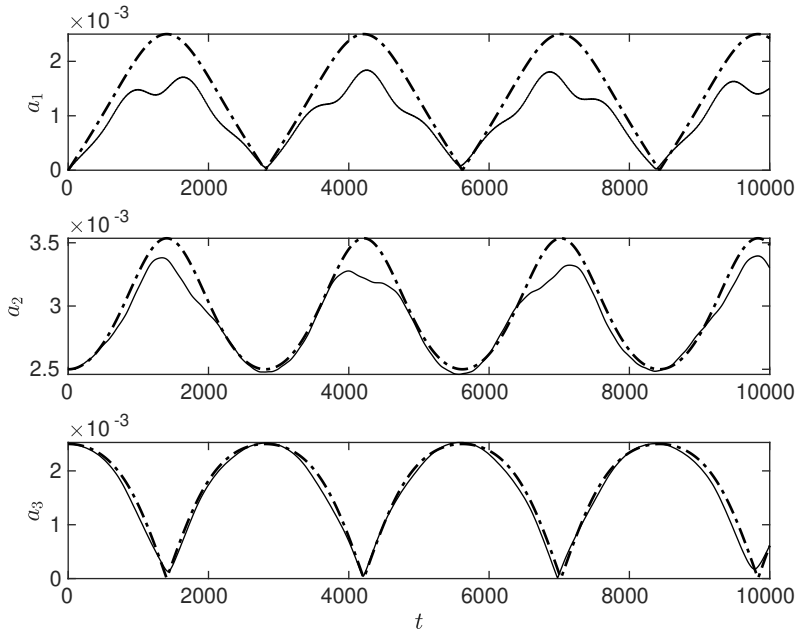

Figure 11: Experiment 2: the first three Fourier modes versus time t computed by the full Euler equations (solid curves) and predicted by the resonance equations (3.6) (dashed-dotted curves).

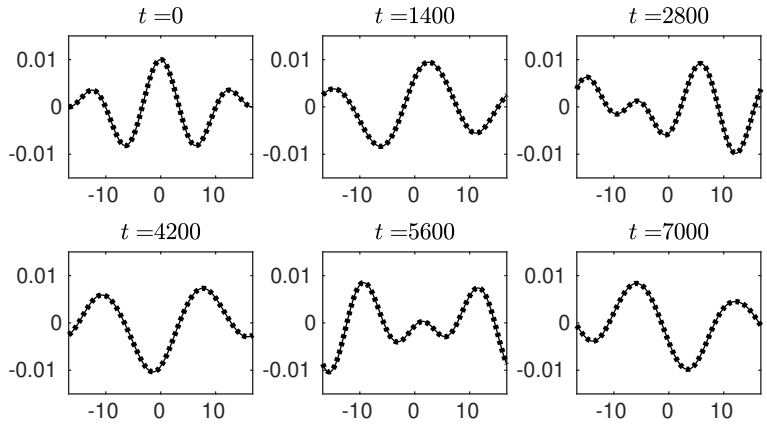

Figure 12: Experiment 2: snapshots of wave profiles of (X, Y) (solid curves) and (X^+, Y^+) (dotted curves).

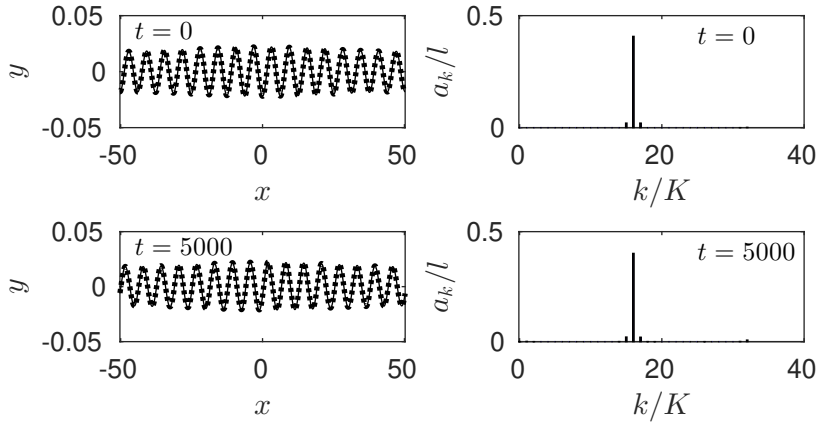

Figure 13: Experiment 3: modulational stable regime (defocusing NLS). (Left) the solid and dotted curves are the snapshots of (X, Y) and (X^+, Y^+), respectively. (Right) the associated Fourier spectra.

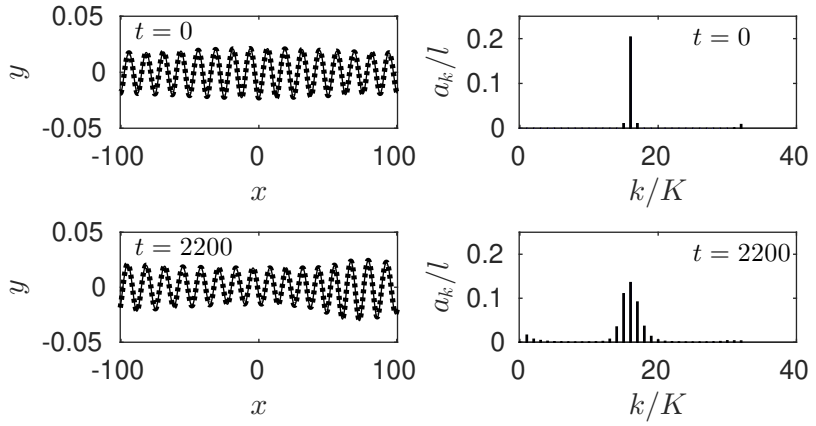

Figure 14: Experiment 4: modulational unstable regime (focusing NLS). (Left) the solid and dotted curves are the snapshots of (X, Y) and (X^+, Y^+), respectively. (Right) the associated Fourier spectra.

The dynamics of the periodic waves in experiments 3 and 4 are presented in Figures 13 and 14, respectively. In the latter, the sideband noise grows in time. Eventually, it becomes no longer negligible compared to the dominant Fourier mode as shown in the right panel, and therefore a modulational instability is observed in experiment 4. Such phenomenon does not occur in Figure 13, i.e., no modulational instability is found in experiment 3. The results agree with the predictions of the NLS equation.

Next, we study the modulational instability of two resonant cases, second harmonic resonance and long-short wave interaction, by numerical simulations of the electrified Euler equations. As previously discussed at the end of section 3.2, the NLS becomes singular in these two resonant cases, so model equations have been derived using different scaling in sections 3.1.1 and 3.1.2. No amendment is required in the numerical scheme on these special occasions since there is no restriction in computing in the fully nonlinear regime. Experiments with the following settings are conducted:

5. $k = k_s = 0.2810$, $K = k_s/16 = 0.0176$, $L = 357.8047$, $a = 0.05$, $N = 4096$, and $dt = 0.002$;

6. $k = k_l = 0.5668$, $K = k_l/16 = 0.0354$, $L = 177.3721$, $a = 0.02$, $N = 4096$, and $dt = 0.001$.

In particular, the modulational wavenumber selected in experiment 6 is less than the associated threshold value K^* (=0.2979) defined in (3.20), namely the

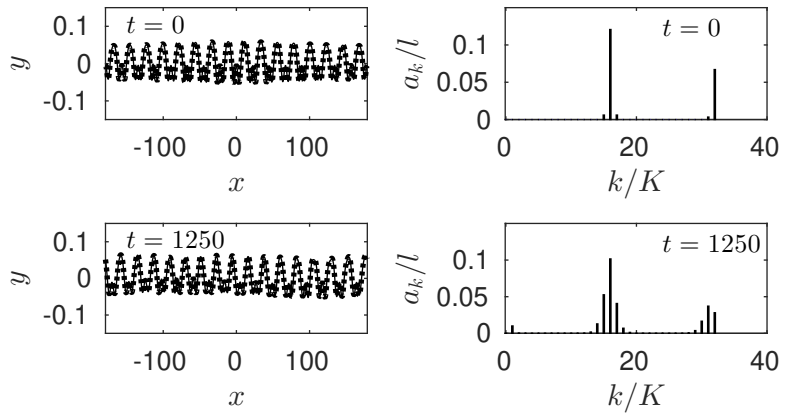

Figure 15: Experiment 5: instability of Wilton Ripples. (Left) the solid and dotted curves are the snapshots of (X, Y) and (X^+, Y^+), respectively. (Right) the associated Fourier spectra.

model equations (3.17) and (3.19) are in the unstable regime. The computational results are plotted in Figures 15 and 16, where modulational instabilities are observed for both cases confirming the predictions by the weakly nonlinear theories presented in sections 3.1.1–3.1.2. The other Wilton-Ripples type solution (b) from Figure 7 has a qualitatively similar behaviour as the one demonstrated in Figure 15, i.e., instability appears for a sufficiently small modulational wavenumber K.

6. Conclusion

The work concerns capillary-gravity waves propagating on a conducting fluid of finite depth under vertical electric fields. The aim is to investigate the impact of the normal electric fields on the nonlinear wave interactions in this context. Model equations have been derived in the weakly nonlinear regime for different asymptotic limits. They are the general resonant triad, second harmonic resonance, long-short wave interaction, and a special resonant quartet. The envelope dynamics of a modulated single-mode wavetrain (a special kind of quartet) are usually governed by the cubic nonlinear Schrödinger equation. However, it becomes singular at two resonant cases, so new scaling needs to be invoked, which results in the second harmonic resonance and long-short wave interaction. The two resonant cases have been shown to transition from 3-wave interactions to 4-wave interactions and vice versa. Computations of the primitive electrified

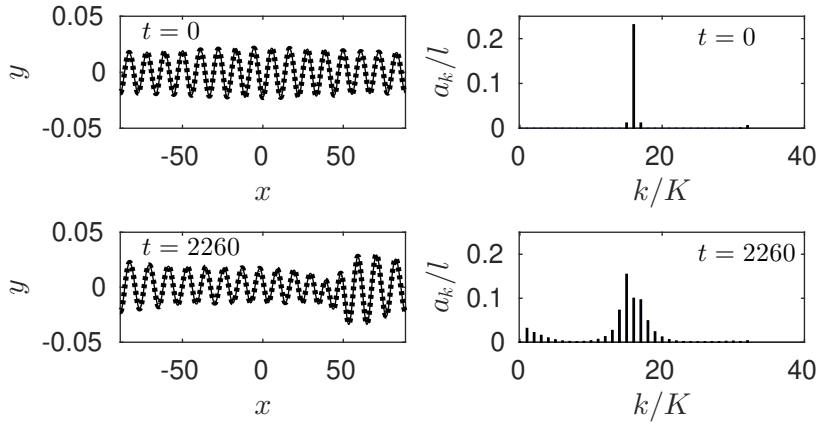

Figure 16: Experiment 6: instability at the occasion of long-short wave interaction. (Left) the solid and dotted curves are the snapshots of (X, Y) and (X^+, Y^+), respectively. (Right) the associated Fourier spectra.

Euler equations have been achieved by a numerical method based on a time-dependent conformal mapping combined with an interpolation technique. A number of numerical experiments have been conducted, and the results agree well with the predictions by the weakly nonlinear theories. The dynamics of solitary waves with very high nonlinearities in this context are still challenging and merit a thorough investigation. Also, the dynamics of a two-layered problem with two fluids of finite density, such as internal waves, is of great interest in future studies.

Acknowledgement

This work was supported by the National Key R&D Program of China under grant 2021YFA0719200 and the Key Program of the National Natural Science Foundation of China under grant 12132018.

References

[1] J.R. Melcher, G.I. Taylor, Electrohydrodynamics: A review of the role of interfacial shear stresses. *Annu. Rev. Fluid Mech.* **1** (1969) 111–146.

[2] D.T. Papageorgiou, Film flows in the presence of electric fields. *Ann. Rev. Fluid Mech.* **51** (2019) 155–187.

[3] G. Taylor, A. McEwan, The stability of a horizontal fluid interface in a vertical electric field. *J. Fluid Mech.* **22**(1) (1965) 1–15.

[4] J.R. Melcher, W.J. Schwarz, Interfacial relaxation over stability in a tangential electric field. *Phys. Fluids* **11**(12) (1968) 2604–2616.

[5] L.L. Barannyk, D.T. Papageorgiou, P.G. Petropoulos, Suppression of Rayleigh-Taylor instability using electric fields. *Math. Comp. Simul.* **82** (2012) 1008–1016.

[6] R. Cimpeanu, D.T. Papageorgiou, P.G. Petropoulos, On the control and suppression of the Rayleigh-Taylor instability using electric fields. *Phys. Fluids* **26** (2014) 022105.

[7] X. Guan, Z. Wang, Interfacial electrohydrodynamic solitary waves under horizontal electric fields. *J. Fluid Mech.* **940** (2022) A15.

[8] N.M. Zubarev, E. Kochurin, Nonlinear dynamics of the interface between fluids at the suppression of Kelvin-Helmholtz instability by a tangential electric field. *JETP Lett.* **104** (2016) 275–280.

[9] T. Gao, P.A. Milewski, D.T. Papageorgiou, J.-M. Vanden-Broeck, Dynamics of fully nonlinear capillary–gravity solitary waves under normal electric fields. *J. Eng. Math.* **108** (2018) 107–122.

[10] T. Gao, A. Doak, J.-M. Vanden-Broeck, Z. Wang, Capillary-gravity waves on a dielectric fluid of finite depth under normal electric field. *Eur. J. Mech. B/Fluids* **77** (2019) 98–107.

[11] C. Easwaran, Solitary waves on a conducting fluid layer. *Phys. Fluids* **31** (1988) 3442–3443.

[12] H. Gleeson, P. Hammerton, D.T. Papageorgiou, J.-M. Vanden-Broeck, A new application of the Korteweg-de Vries Benjamin-Ono equation in interfacial electrohydrodynamics. *Phys. Fluids* **19** (2007) 031703.

[13] Z. Wang, Modelling nonlinear electrohydrodynamic surface waves over three-dimensional conducting fluids. *Proc. R. Soc. A* **473** (2017) 20160817.

[14] Z. Lin, Y. Zhu, Z. Wang, Local bifurcation of electrohydrodynamic waves on a conducting fluid. *Phys. Fluids* **29** (2017) 032107.

[15] A. Doak, T. Gao, J.-M. Vanden-Broeck, J.J.S. Kandola, Capillary-gravity waves on the interface of two dielectric fluid layers under normal electric fields. *Quart. J. Mech. Appl. Math.* **73**(3) (2020) 231–250.

[16] O.M. Phillips, On the dynamics of unsteady gravity waves of finite amplitude. I: The elementary interactions. *J. Fluid Mech.* **9**(2) (1960) 193–217.

[17] V.E. Zakharov, Stability of periodic waves of finite amplitude on the surface of a deep fluid. *J. Appl. Mech. Tech. Phys.* **9** (1968) 190–194.

[18] D.J. Benney, A.C. Newell, The propagation of nonlinear wave envelopes. *J. Math. Phys.* **46**(1-4) (1967) 133–139.

[19] L.F. McGoldrick, Resonant interactions among capillary-gravity waves. *J. Fluid Mech.* **21** (1965) 305–331.

[20] W.F. Simmons, A variational method for weak resonant wave interactions. *Proc. R. Soc. Lond. A* **309**(1499) (1969) 551–577.

[21] K.M. Case, S.C. Chiu, Three-wave resonant interactions of gravity-capillary waves. *Phys. Fluids* **20**(5) (1977) 742–745.

[22] L.F. McGoldrick, On Wilton's ripples: a special case of resonant interactions. *J. Fluid Mech.* **42**(1) (1970) 193–200.

[23] D.J. Benney, A general theory for interactions between short and long waves. *Stud. Appl. Math.* **56**(1) (1977) 81–94.

[24] V. D. Djordjevic, L. G. Redekopp, On two-dimensional packets of capillary-gravity waves. *J. Fluid Mech.* **79**(4) (1977) 703–714.

[25] W. Craig, P. Guyenne, & C. Sulem (2012). The surface signature of internal waves. *J. Fluid Mech.*, *710*, 277–303.

[26] A. I. Dyachenko, V. E. Zakharov, E. A. Kuznetsov, Nonlinear dynamics of the free surface of an ideal fluid, *Plasma Phys. Rep.* **22**(10) (1996) 829–840.

[27] A.D.D. Craik, *Wave Interactions and Fluid Flows*. Cambridge University Press (1985).

[28] D.J. Kaup, The solution of the general initial value problem for the full three-dimensional three-wave resonant interaction. *Physica D* **3**(1-2) (1981) 374–395.

[29] M.C.W. Jones, Nonlinear stability of resonant capillary-gravity waves. *Wave Motion* **15**(3) (1992) 267–283.

[30] T. Gao, P.A. Milewski, Z. Wang, Capillary-gravity solitary waves on water of finite depth interacting with a linear shear current. *Stud. Appl. Math.* **147**(3) (2021) 1036–1057.

[31] P.A. Milewski, J.-M. Vanden-Broeck, Z. Wang, Dynamics of steep two-dimensional gravity-capillary solitary waves. *J. Fluid Mech.* **664** (2010) 466–477.

[32] J.-M. Vanden-Broeck, *Gravity-capillary free-surface flows*. Cambridge University Press. (2010).

[33] M. Tanaka, Maximum amplitude of modulated wavetrain. *Wave Motion* **2**(6) (1990) 559–568.